arXiv:astro-ph/0209010v1 1 Sep 2002

Chandra and XMM Observations of the ADC Source 0921-630

T. R. Kallman[1], L. Angelini[1,2], B. Boroson[3] and J. Cottam[1]

ABSTRACT

We analyze observations of the low mass X-ray binary 2S0921-63 obtained with the gratings and CCDs on Chandra and XMM. This object is a high inclination system showing evidence for an accretion disk corona (ADC). Such a corona has the potential to constrain the properties of the heated accretion disk in this system, and other LMXBs by extension. We find evidence for line emission which is generally consistent with that found by previous experiments, although we are able to detect more lines. For the first time in this source, we find that the iron K line has multiple components. We set limits on the line widths and velocity offsets, and we fit the spectra to photoionization models and discuss the implications for accretion disk corona models. For the first time in any ADC source we use these fits, together with density constraints based on the O VII line ratio, in order to constrain the flux in the medium-ionization region of the ADC. Under various assumptions about the source luminosity this constrains the location of the emitting region. These estimates, together with estimates for the emission measure, favor a scenario in which the intrinsic luminosity of the source is comparable to what we observe.

1. Introduction

In spite of much study, understanding of the geometry of the gas flows and circumstellar gas in low mass X-ray binaries, (LMXBs) remains uncertain. The conventional picture consisting of a neutron star, low mass companion, and accretion disk is heavily influenced by analogy with cataclysmic variables. There are fewer direct observational constraints on the accretion disks in LMXBs than in other accretion driven systems. A major contributor to this uncertainty is the influence of X-ray heating, which makes circumstellar gas a mirror for X-rays rather than a medium which can be studied via its intrinsic emission. In

[1]NASA Goddard Space Flight Center, LHEA, Code 665, Greenbelt, MD 20771

[2]University Space Research Association

[3]Harvard-Smithsonian Center for Astrophysics, 60 Garden St., Cambridge MA 02138

addition, dilution of the circumstellar emission by the strong continuum emanating from the neutron star adds to the difficulty of finding signatures of the disk or other structures in the spectrum.

Useful clues to the geometry of LMXBs may be provided by the sources in which we are likely observing close to the plane of the accretion disk and binary orbit. These sources may play a role in our understanding of LMXBs which is analogous to the role played by Seyfert 2 galaxies in the understanding of active galaxies; the configuration of the circumstellar gas can be studied when the direct X-rays from the continuum source are at least partially blocked. In such high inclination systems the presence of partial eclipses by the secondary star suggest the presence of an extended component of X-ray emission, likely due to scattering and emission from a cloud of highly ionized gas. The X-rays from the neutron star may provide sufficient heating and ionization to account for the properties of this accretion disk corona, or ADC (Begelman, Mckee and Shields 1982; Begelman and McKee 1983). In addition, the heated gas may flow outward in a wind (Woods et al., 1996; Proga and Kallman 2002) which can potentially affect the mass budget of the system. The existence of accretion disk coronae has been substantially confirmed, and the column density and size have been constrained, by fitting of models to observed X-ray light curves. Simple models treat the corona as a spherical cloud (White and Holt, 1982; McClintock, et al., 1982; Mason, 1986) in which the X-rays are reflected into our line of sight by scattering alone. These models have also constrained the size and shape of the outer rim of the accretion disk, although the results depend on the assumed geometry for the ADC.

In addition to scattering continuum photons, the corona should also radiate in atomic emission features arising from partially ionized material. Such emission has been predicted by, e.g. Kallman and White (1989), and by Vrtilek, Soker and Raymond (1994), Ko and Kallman (1994). Strong line emission is expected under a variety of assumptions, and that the line emission (as measured by equivalent width) is strongest when the inclination of the binary system is closest to 90^o. Observations of line emission have the potential to provide a sensitive test of the hypothesis that the corona is heated and ionized entirely by X-rays from the central neutron star, since the ionization balance and emission measure together serve to constrain both the gas density and the size of the emission region.

In order to carry out such a test we have used the gratings and CCD detectors on both the Chandra and the XMM satellites to observe the eclipse spectrum of 2S0921-63, a well known LMXB which shows the approximately sinusoidal lightcurve indicative of an accretion disk corona. Its period of 9.01 days makes it one of the longest period LMXB systems, and also makes it particularly suitable for eclipse studies owing to the duration of the eclipse. EXOSAT observations of the spectrum through an orbital cycle (Mason

et al. 1987) showed that the spectrum softens during eclipse. The spectrum was fit to a hard power law, with a photon index of 1.16, and a column density of 1.4×10^{21} (although Mason et al. find evidence for contamination at low energies which makes this value somewhat uncertain). The eclipse ($\leq 50\%$ of the uneclipsed flux) lasted approximately 80 ksec. The relatively low X-ray to optical flux ratio and many recorded optical dips (e.g. Branduardi-Raymont et al., 1981, 1983; Chevalier and Ilovaisky, 1981, 1982) are further evidence for a hidden X-ray source. Cowley et al. (1982) estimate the distance to be $\simeq$7 kpc, implying a luminosity of 2.4 $\times10^{35}$ erg s^{-1}.

2S0921-63 was observed with ASCA on several occasions, including a total of 27 ksec of good data obtained during eclipse. Fits to these data reveal a hard power law continuum and column density comparable to those observed by EXOSAT. This spectrum is significantly harder than the spectra typically observed from low inclination LMXB systems. The spectrum contains an iron K line at an energy of 6.75 keV, intermediate between the He-like and H-like ionization states of this element. This line is unique among LMXBs for its equivalent width; both ASCA and EXOSAT (Asai, 2000; Gottwald et al., 1996) measure $\simeq$ 120eV for this quantity, while typical LMXBs show much weaker lines, $\sim 40 - 80$ eV. The flux in the 2-10 keV band in the ASCA spectrum of 2S0921-63 is 3.2 $\times10^{-11}$ erg cm^{-2} s^{-1}. In addition, the ASCA spectrum contains evidence for line emission in the 0.5-2 keV band, not previously published.

In the following sections we describe our observations of this source using Chandra and XMM, the extraction and analysis procedures, results of model fits, and their implications for understanding of 2S0921-63 and for ADC sources in general.

2. Observations

2.1. Chandra

2S0921-630 was observed by Chandra using the HETG and ACIS-S detector between UT 15:23:49 2001-08-02 and UT 13:01:13 2001-08-03. The observation lasted approximately 74000 seconds. In order to best eliminate the influence of any direct X-rays from the neutron star, the observation was centered on eclipse phases 0.97 – 1.07, based on the ephemeris: $\phi = \mathrm{JD2446249.18}^{+}_{-}0.01 + n \times 9.0115^{+}_{-}0.0005$ (e.g. Mason et al., 1987). Although the eclipse light curve is gradual, an observation of this duration fits within the time when the flux is less than $\simeq 60\%$ of the uneclipsed value.

Figure 1 shows the HEG and MEG light curves during our observation, plotted against orbital phase using the ephemeris of Mason et al (1987). The data have been binned into

100 second bins. A secular variability is apparent, resulting in a factor $\simeq$2 increase in the counting rate between the beginning and the end of the observation. This variability is more pronounced in the MEG than in the HEG, suggesting that the orbital modulation is stronger at lower energies. The statistical quality of the HETG spectrum is not sufficient to allow sensitive searches for spectral variability associated with this increase. The mean first order counting rates were .19 counts/s in the HEG and 0.33 counts/s in the MEG. Data was reduced using the standard analysis pipeline and Ciao. We add the + and - first order spectra together and analyze only these orders. The zero order ACIS-S spectrum showed clear evidence of pileup and will not be discussed further in this paper. The spectra from the HEG and MEG were fitted simultaneously, using the xspec package (Arnaud 1996). Best fit values are found by minimizing the value of the C statistic. Here and in the fitting of the XMM data we quote the values of best fit parameters together with the errors derived from stepping the parameter in question and determining the Δ C statistic or $\Delta\chi^2$=10 value. All model fits attempt to account for the ACIS low energy quantum efficiency contamination by using the acisabs model in the post-release version of xspec 11.2.

2.2. XMM-Newton

2S0921-630 was observed by XMM-Newton between UT 11:39:00 2000-12-20 and UT 03:24:49 2000-12-21. Data were taken simultaneously for the EPIC detectors MOS and PN (using the medium filter) and with the RGS. All data were processed with the XMM-Newton Science Analysis Software, SAS 5.3, with the corresponding calibration files available for that version. The RGS covers a wavelength range of approximately 6 to 38 $\AA$ (E=0.35 – 2.5 keV) with a resolution of 0.05 $\AA$ and a peak effective area of about 140 cm^2 at 15 $\AA$ (0.826 keV). The observation was separated into two intervals, one lasting 7334 seconds, and a second lasting 61878 seconds. Here we discuss only the data from the second interval. Figure 2 shows the light curve of the PN counts, plotted against orbital phase using the ephemeris of Mason et al (1987). The shape of this curve corresponds crudely to the shape of the Chandra HETG lightcurve in the local maximum near phase 0.965, minimum near 1.01, and overall secular increase. The mean counting rate was .25 counts/s in RGS 1 and 0.32 counts/s in RGS 2. The first order spectra from the RGS 1 and 2 are fitted simultaneously, using the xspec package (Arnaud 1996).

3. Results

3.1. ASCA

The results from fitting to the low energy portion of the ASCA spectrum have not been previously published, and so we present them here prior to the presentation of the other results. The results of fitting the 27 ksec of data contained during eclipse on 04-05-1994 06:09:12 are shown in Table 1. The spectrum was fit to a cutoff power law plus narrow Gaussian emission features. The energies of the features are consistent with those expected from the Lα and Lβ lines of Ne X, and the Lα lines of Si XIV and S XVI. The O VIII Lα line is not statistically significant in this spectrum. In addition, the fit requires a (single) iron K line at 1.82 $\AA$ (6.8 keV), corresponding approximately to the He-like ionization state of this element. The measured width of this line is 0.5 keV (Asai et al. 2000), which is likely due to the effects of blending. These results foreshadow those found by the other instruments described in this paper.

3.2. Chandra HETG

In order to better understand the contributions of various components to the spectrum we fit the data from all the various instruments with several trial model spectra, with progressing physical sophistication. The simplest model consists of a single power law plus absorption by neutral material. The results of such a fit to the Chandra HETG data are shown in Table 2. Figure 3 shows the ratio of the data to the model for such a fit. The HEG and MEG are plotted separately. The spectra have been binned for the purpose of plotting only. The best fit power law index (γ) is $1.01^{+0.15}_{-0.9}$, which is consistent with that found by ASCA. The neutral column is 1.6 $\times 10^{21}$ cm^{-2}, which is similar to that found by EXOSAT averaged over orbital phase. This value is affected by the treatment of the acis contamination in xspec; when the acisabs model is omitted from the analysis the inferred column increases to 2.05 $\times 10^{21}$ cm^{-2}, other parameters are unchanged.

Figure 3 shows that, although the fit to the continuum is adequate in the Chandra 1-15 $\AA$ (0.8 - 7 keV) region, there are significant residuals near 12, 10.6, 8.4, 7.1, 6.2, 4.7, and 1.7-1.9 $\AA$ (1, 1.3, 1.44, 1.72, 2, 2.6, 6.4 – 7 keV), which correspond to emission lines due to Ne X Lα, Ne X Lβ, Mg XII Lα and Lβ, Si XIV Lα, S XVI Lα, and Fe I-XXVI, respectively. Not all of these lines are statistically significant; Table 2 shows the effect of adding multiple narrow Gaussian lines to the absorbed power law model at the energies of the significant lines. This results in a reduction of the C statistic from 9390 to 9009 for 8384 PHA bins. All the line fits are consistent with narrow lines ($\sigma \leq 0.005$ for the stronger lines), corresponding to Doppler widths less than 1500 km/s. The flux in the 2-10 keV band in this spectrum is 3.8 $\times 10^{-11}$ erg cm^{-2} s^{-1}. Also given in table 2 and all later tables are

the line IDs, and the log of the probability of random occurrence according to an F test.

The HETG spectrum can also be fitted by a detailed atomic simulation of a photoionized gas. This was done using models calculated with the XSTAR code (see, e.g. Kallman and Bautista, 2000; Kallman et al., 1996), which assumes that the gas is optically thin, and that the ionization is solely due to continuum X-rays from the neutron star. Such fits constrain the ionization parameter and normalization to be $\log(\xi) \simeq 4.5$ and $\simeq 300$, respectively. Figure 3 and Table 3 show the best-fit model. The statistical quality of the fit is significantly better than for the Gaussian fits, C statistic=8731 for 8384 PHA bins. The statistical quality of the data is not sufficient to tightly constrain the abundances of the emitting ions; formally we obtain 0.1, 0.28, 0.30, 0.33, 0.16, 0.25, 0.22, 2.3e-3, for O, Ne, Mg, Si, S, Ar, Ca, Fe, respectively, relative to solar (Grevesse et al., 1996).

3.3. XMM

The XMM data includes the two grating datasets, two EPIC-MOS, and the EPIC-PN. Of these, the RGSs provide high resolution ($\varepsilon/\Delta\varepsilon \sim 300$) over the 0.5 – 2 keV energy band, while the EPIC detectors provide moderate resolution ($\varepsilon/\Delta\varepsilon \sim 20 - 50$) over the 0.5 – 10 keV energy band. Owing to pileup of the Chandra zero order, the EPIC spectra provide our only insight to the broad-band spectrum of 2S0921-63.

3.3.1. EPIC-MOS

The MOS provides moderate energy resolution and sensitivity over the entire XMM energy band. Figure 5 shows a fit to the global spectrum obtained using a single power law with neutral absorption, both the measured and modeled counts and the ratio of data to model. Although we have fitted to both MOS detectors simultaneously, only MOS 1 is shown in this figure for clarity. This shows that the global shape of the spectrum is adequately reproduced, and that there are residuals near 6.5-7 keV corresponding to the iron K lines, in addition to smaller residuals at lower energies, 0.5 – 2 keV, corresponding to the K lines from medium-Z elements. In Table 4 we show the parameters of the power law only fit, and for a fit to a power law plus Gaussians at the energies of the iron K lines. We defer a discussion of the K lines from medium Z elements to the section on RGS fitting. Table 4 shows that the energies of the iron lines are consistent with those of the He-like line near 1.82 $\AA$ (6.8 keV), and the H-like line at 1.78 $\AA$ (6.97 keV). The neutral-like fluorescence line (Fe I-XVII) at 1.94 $\AA$ (6.4 keV) appears in the residuals but

is not statistically significant in this fit. The ratios of the strengths of the lines, and their energies, are consistent with those found by the Chandra HETG. The flux in the 2-10 keV band in this spectrum is 5.9 $\times 10^{-11}$ erg cm^{-2} s^{-1}.

3.3.2. EPIC-PN

The PN provides superior energy resolution and sensitivity at higher energies, but owing to calibration uncertainties we can find no satisfactory fit to the global spectrum is obtained using any of the spectral shapes that we use for any of the other detectors. In order to avoid this problem, and still make use of the high energy part of the spectrum, we fit the PN spectrum only at energies between 5 and 10 keV. In this energy band we are able to obtain acceptable fits. The counting rate is 15.2 counts s^{-1} in this energy band. The upper panel of figure 6 shows the ratio of the PN spectrum to a simple model consisting of a power law with index 1.2. This shows residuals at the energies of the 3 iron lines found by the MOS and the Chandra HETG, but in addition there is a monotonic decrease in flux above 7 keV, and emission features at energies above 7.1 keV. This spectrum appears superficially very similar to the ASCA spectrum of 4U1822-30 in this energy range (White, 1996). This spectrum does not show the behavior expected from Compton reflection, which is a flattening of the power law at high energies. Instead, the spectrum is apparently steepening between 7 and 10 keV and contains narrow features which are statistically significant. We obtain an acceptable fit this spectrum to a power law with index 1.2 and a cutoff at 7 keV, Gaussians at the energies of the iron lines: 1.94, 1.85, and 1.78 $\mathring{A}$ (6.4, 6.7, and 6.97 keV), plus additional Gaussian emission lines at 1.59 and 1.51 $\mathring{A}$ (7.8 and 8.2 keV). This model fit gives χ^2/ν=874/1028. We have also tested this model against the MOS data in this energy range and found it to be acceptable. We have tried fitting this portion of the spectrum to a single power law plus atomic absorption as might be expected from an iron K edge or ensemble of edges. The best fit to a single power law continuum plus Gaussian emission at the energies of the iron Kα lines has absorption edges at 7.1 and 8.4 keV. This results in a fit which has χ^2/ν=902/1032, which is significantly greater than the fit to a curved continuum plus Gaussian emission. The reason for this is the presence of narrow features at 1.59 and 1.51 $\mathring{A}$ (7.8 and 8.2 keV).

The 1.59 $\mathring{A}$ (7.8 keV) line wavelength corresponds approximately to that of the 1-3 resonance line of Fe XXV, or to the 1-2 resonance line of He-like Ni. The 1.51 $\mathring{A}$ (8.2 keV) line is consistent with the 1-4 resonance line of Fe XXV, although its strength relative to that of the 1.85 $\mathring{A}$ (6.7 keV) 1-2 line is greater than expected if this is the correct identification. We can clearly rule out the Kα line of Cu, at 1.54 $\mathring{A}$ (8.05 keV), which is an

instrumental feature known to appear in some PN datasets. The results are shown in the lower panel of figure 6 and Table 5. The PN data allows a constraint of the widths of the iron K lines; for the 1.94 $\AA$ (6.4 keV) line we can marginally exclude velocities less than .15 keV, corresponding to Doppler velocities $\simeq$ 7000 km s$-$1, and for the 1.78 $\AA$ (6.97 keV) line we can exclude Doppler velocities less than 430 km s^{-1} and greater than 3900 km s^{-1}.

3.3.3. RGS

Our procedure for fitting to the XMM RGS spectra is similar to that used for the Chandra HETG. One difference is that xspec encounters numerical problems when using the C statistic with RGS data, so we have rebinned the RGS data using the ftools tool grppha in order to have at least 20 counts per bin, and then used χ^2 statistics. The results of fitting to various models are shown in Table 6. Figure 7 shows the ratio of the data to the model for the simplest fit, that of a single power law plus neutral absorption. The spectra have been binned for the purpose of plotting only. The power law index has been forced to the value found by the fits to the MOS detectors. For this fit χ^2/ν is 1522/1672. Figure 7 shows that there are significant residuals near 22, 19, 16 12, 10.6, 10., and 8.6 $\AA$ (0.59, 0.65, 0.78, 1, 1.2, and 1.44 keV), which correspond to emission lines due to O VII 1-2, O VIII Lα, O VIII Lβ, Ne X Lα, Ne X Lβ, and Mg XII Lα, respectively. In addition there are significant features at 22.9 and 23.1 $\AA$ which do not have secure identifications. The parameters of a fit to the spectrum with Gaussian emission lines added at these energies is shown in the second column of Table 6. Inclusion of the narrow Gaussian lines results in a reduction in χ^2/ν to 1392/1684. Also given in table 6 are the line IDs, and the log of the probability of random occurrence according to an F test. The spectral resolution of the RGS results in upper limits on the widths of the Gaussians which are greater than for the Chandra HETG. A notable difference between the Chandra spectrum and that shown here is the presence of the He-like O VII lines at 21.8 $\AA$ and 22.1 $\AA$ (0.569 and 0.561 keV). These correspond to the intercombination and forbidden lines, respectively, and their best-fit intensity ratio is 1.3. From this we infer that the predominant emission mechanism is recombination, rather than collisional excitation or resonance scattering, since either of these mechanisms is expected to produce strong permitted emission at 21.6 $\AA$ (0.574 keV). In addition, the comparable strengths of the forbidden and intercombination components implies a density in the range 10^9 – 10^{11} cm^{-3} (eg. Bautista and Kallman 1999; Porquet and Dubau 1999). At greater densities the forbidden component is expected to be collisionally deexcited, while at lower densities the intercombination line is weaker owing to the more efficient cascades to the upper level of the forbidden line.

Table 7 and Figure 8 show the result of fitting the RGS data to an xstar model. We again force the continuum slope to match that of the MOS spectrum. We fit to a two component model, one component with log(ξ)=1 and one with log(ξ)=4.5, in order to simultaneously fit the low and high ionization lines in the RGS spectrum. The statistical quality of the fit is significantly better than for the Gaussian fits, χ^2/ν=1418/1670. This fit differs from the results of the xstar fits to the Chandra HETG spectra, for which we found an acceptable fit to a single ionization parameter, log(ξ)=4.5. An indicator of the difference is the O VII 1-2 line near 21 $\mathring{A}$ (0.59 keV), since this line requires lower ionization parameter in order to be emitted efficiently. Figure 8 shows that this 2 component model adequately accounts for the spectrum in the 15-30 $\mathring{A}$ (0.4 – 0.8 keV) range, but that there are inconsistencies between the model and the data in 8 - 15 $\mathring{A}$ (0.8 – 1.6 keV) range. Most notable is the feature near 9.7 $\mathring{A}$ (1.28 keV) which may be identified with Ne X Lβ. This feature has a strength which is comparable to the Ne X Lα line at 10.2 $\mathring{A}$ (1.22 keV) and which is greater than can be produced by recombination or collisional excitation. The narrow features near 10.8, 11.25, 11.45, and 11.7 $\mathring{A}$ (1.148, 1.110, 1.083, and 1.060 keV) are not statistically significant, and so are not fitted by the xstar model. It is also worth noting the Ne IX 1-2 lines near 13.5 - 13.7 $\mathring{A}$ (0.9 – 0.92 keV) which appear to be consistent with the predictions of the xstar model. The best-fit abundances for this model are: O:Ne:Mg=0.3:1.6:2.1

The differences in the best-fit ionization parameters found from fitting to Chandra and XMM can be entirely attributed to the differing bandpasses of the two instruments. The Chandra HETG detects such high ionization lines as S XVI and Si XIV Lα, which are outside the bandpass of the XMM RGS and which are only emitted efficiently at high ionization parameter. The RGS detects the O VII 1-2 lines which are outside the Chandra bandpass and which require a lower ionization parameter for efficient emission. We have verified that this is the origin of the discrepancy by fitting both instruments to only the region of wavelength for which both have significant sensitivity, 7 – 14 $\mathring{A}$ (0.88 – 1.77 keV). The result is that both fit equally well over a broad range of ionization parameter, since both the high ionization and low ionization lines have been excluded in this fit.

4. Discussion

4.1. Velocity Offsets and Widths

In figure 9 we compare the velocity offsets of the lines observed by the various instruments. The velocity offsets are determined using line wavelengths from the NIST database, where available, and from the compilation of Verner (1999) for the others. Figure

9 shows that essentially all the line wavelengths are consistent with being emitted at zero velocity, although the uncertainties are typically ∼1000 km/s or greater. Only the wavelength of the Fe XXVI Lα near 1.78 $\AA$ (6.97 keV) as measured by the Chandra HETG is inconsistent with zero velocity, although the wavelength of this line as measured by the XMM PN is consistent with zero velocity. In the case of the line observed at 1.85 $\AA$ (6.7 keV) we include the data for all 3 of the components of the 1-2 lines of Fe XXV, with the result that the wavelengths of the forbidden and semi-forbidden lines are consistent with smaller velocity offsets than the allows line. This suggests that, if the line-emitting material does not have a high bulk velocity relative to us, then the lines are formed predominantly by recombination.

The limits on line widths allow us to approximately constrain the location of the line emitting gas, under the assumption that the gas motions are Keplerian in the vicinity of a 1 $M_\odot$ compact object. If so, the limits on the velocity obtained for the 1.78 $\AA$ (6.97 keV) line using the XMM PN correspond to a radii between 8.8 $\times 10^8$ cm and 7.2 $\times 10^{10}$ cm. Although there are no independent measures of the mass, it is likely that the inclination i is close to 90^o. This can be compared with estimates for the disk outer radius. Using standard expressions for the Roche lobe radii (eg. Frank, King and Raine, 1992), and assuming values for the mass ratio q in the range 1 – 2.2 (Shabhaz et al., 1999) the radius of the compact object Roche lobe is in the range 0.9 – 1.2 $\times 10^{12}$ cm. Although estimates for the disk radius itself are less certain, it is clear that the iron emission originates at a small fraction ($\sim 10\%$) of the probable outer disk radius. The width of the 1.94 $\AA$ (6.4 keV) iron Kα line measured by the XMM PN is much greater, 0.27 keV. This corresponds to the Keplerian broadening at a disk radius of 7×10^7 cm. This difference in widths is surprising if it actually reflects the range of radii where the lines are emitted. A more likely explanation is that the width of the 1.94 $\AA$ (6.4 keV) line is due to blending of multiple components of the fluorescence lines from various ionization stages of iron. If so, the estimate of radius obtained from the 1.78 $\AA$ (6.97 keV) line remains relevant.

4.2. Line Luminosities, Variability, and Emission Measures

The fluxes we derive for the various experiments are 5.4, 3.8, and 5.9 $\times 10^{-11}$ erg cm^{-2} s^{-1} in the 2-10 keV band for ASCA, Chandra, and XMM respectively. The fact that the ASCA and XMM are consistent, and that the Chandra flux is slightly lower, further confirms the conclusion that the fact that the Chandra spectrum requires only a high ionization parameter component while the XMM RGS requires both high ad low ionization parameter components is not due to variability. The lower ionization parameter inferred

from the XMM fit would suggest a lower flux during the XMM observation if variability were the origin for the difference. However, the difference is in the opposite direction, and the Chandra observation has lower flux. From this we conclude that the difference in the best fit ionization parameter for the two observations is due to the differing wavelength bands of the two instruments together with an intrinsic distribution in ionization parameter within the source, rather than variability.

Figure 11 shows the emissivities for the various lines we observe as a function of ionization parameter, ξ, as calculated for a library of single-zone xstar photoionization models. Also included in this are lines which we do not detect, and whose absence places constraints on the conditions in the ADC. These include principally the lines of He-like ions such as Ne IX, Mg XII, and Si XIII. From this figure it is clear that the absence of these lines in the Chandra HETG spectra implies ionization parameter values greater than $\xi \sim 10^4$. Conversely, the best fit to the XMM RGS spectrum that we find is affected by the need to fit the O VII line near 21 $\AA$, and this requires ionization parameters $\xi \sim 10^1$.

The line strengths can be used to infer the emission measure of the gas in 2S0921-630 by dividing the line luminosity by the emissivity of the various lines. As example of such a calculation is shown in figure 10, for the various strong lines detected by Chandra and XMM. These estimates were derived by using the line emissivities shown in figure 11, and summing over an arbitrary distribution of ionization parameters binned into 9 bins equally spaced in $\log(\xi)$ from 1 to 5. The result is a model luminosity for each line, $L_i^{mod} = \Sigma_{\xi_k} j_{i,k} EM_k$, where $j_{i,k}$ is the emissivity for line i in ionization parameter bin k as shown in figure 11 and EM_k is the emission measure distribution. This was fit to the observed luminosities and errors L_i^{obs} and σ_i^{obs}, derived from tables 2, 5 and 6 using a distance of 7 kpc by varying the emission measure in each bin independently until a minimum was found in the figure of merit. We take the figure of merit to be to be $\Sigma_i((L_i^{mod} - L_i^{obs})/\sigma_i^{obs})^2$. This procedure is not expected to be highly accurate, owing to the simplified physical assumptions and the coarseness of the various grids, these results in the upper panel of figure 10 show that we are able to fit most line strengths to within a factor of 2. The lower panel of figure 10 shows the derived best-fit emission measure distribution, which corresponds to 3 distinct components. This is similar to the result obtained by fitting xstar models to the Chandra and XMM data separately. This distribution is not consistent with a power law or other smoothly varying function.

An equivalent procedure is to use the normalization calculated using the fit to the xstar model. The general procedure for doing this is outlined in the xstar manual and in the Appendix to this paper. The result is $\sim 10^{57}$ cm^{-3}, which can be compared with that expected from an ADC.

Estimates for the emission measure of an ADC depend on several quantities which are not accurately determined, including the geometry of the corona and its effect on the transfer of radiation, the intrinsic luminosity and spectrum of the continuum X-ray source, the possible role of outflows or winds, and the presence of any other heating or ionization mechanism such as magnetohydrodynamic processes (eg. Stone and Miller, 2001). Simple estimates can be obtained by assuming the corona is hydrostatic and unaffected by MHD processes, as was done by Kallman and White (1989). If so, the corona can be crudely represented as a series of concentric cylinders, each having a Gaussian density distribution with height, and where the local scale height is:

$$z_s(R) = \sqrt{\frac{kTR^3}{GMm_H}}$$

where T is the local gas temperature and M is the mass of the central compact object. The maximum density in the corona is attained when the ionization parameter is $\Xi = \Xi^*_H \simeq$1–10, (eg. Krolik McKee and Tarter, 1981), where $\Xi = L/(4\pi R^2 nckT)$. Then the emission measure is approximately

$$EM(R) \simeq n^2_{max} 4\pi R^2 z_s = 1.2 \times 10^{61} L^2_{38} R^{-1/2}_{10} T^{-3/2}_7 \Xi^{-1} \mathrm{cm}^{-3}$$

where T_7 is the temperature in units of 10^7K, R_{10} is the radius in units of 10^{10} cm, and L_{38} is the continuum luminosity in units of 10^{38} erg s^{-1}. This shows that the emission measures inferred from the photoionization model fits can be attained by an accretion disk corona for a plausible range of parameters, i.e. $L_{38} \sim 10^{-2}$, and all other parameters of order unity.

A further constraint on the ADC comes from the derived density in the O VII lines. If the intrinsic luminosity of the X-ray source is 10^{38} erg s^{-1}, then the minimum distance at which material at the inferred O VII maximum density of 10^{11} cm^{-3} and ionization parameter $\log(\xi) \simeq$2 can exist under photoionization is 2.2×10^{12} cm. This is larger than the likely outer radius of the accretion disk, which is less than $\sim 10^{12}$ cm (see below). This estimate assumes that the local radiation intensity in the ADC is determined by geometrical dilution of the X-rays from the compact object. The most likely explanation is that the intensity of the ionizing continuum radiation within the O VII region of the ADC is reduced by scattering or absorption. If so, the amount of attenuation required in order to reduce the O VII radius to a value consistent with the disk is a factor ∼100. This differs from the simple ADC models which have been constructed by eg. Ko and Kallman (1996) and Jimenez-Garate et al. (2001), in which ionization parameters low enough to produce O VII could only occur at densities $\sim 10^{14}$ cm^{-3} or greater. An alternative explanation is that the

X-ray source is intrinsically faint, $\sim 10^{36}$ erg s^{-1} or less, or that the O VII emission region lies outside the traditional estimates for the disk outer radius.

4.3. Comparison with other LMXBs

Although 2S0921-630 is not the brightest ADC source, it may the the most suitable target for studying the accretion disk corona during eclipse. This is based on the ASCA spectrum, and is likely due to its long orbital period, which allows long observations to be carried out entirely during eclipse. An illustration of this is provided by the spectrum of the ADC source 4U1822-371 (Cottam et al., 2001), which shows many of the same features as 0921-63. However, the line emission from 1822-371 is much weaker in spite of its greater total flux. In addition, in 4U1822 the emission lines don't come from the corona. They are phase-dependent and appear to come from the photo-illuminated bulge at the impact point. This suggests that in 4U1822-371 there may be more dilution of the line emission by directly observed X-rays than is expected, or perhaps the inclination is such that we detect more direct X-rays than in 2S0921-630.

4.4. Neutral-Like Iron line

The iron K line is unique among X-ray lines from abundant elements in that it can be emitted efficiently by neutral or nearly-neutral gas via inner shell fluorescence in addition to being emitted efficiently when iron is highly ionized (here and in what follows we define 'neutral-like' to be ion stages less than Fe XVII, so that the line energy is indistinguishable from neutral). Although many LMXBs (including 2S0921-630) show emission from highly ionized iron, a uniformly illuminated accretion disk is expected to radiate a strong line from nearly neutral iron. The strength of this line is a constraint on the strength of illumination of the accretion disk at radii $\geq 10^8$cm, where the iron in the disk photosphere is expected to neutral-like. A simple estimate for the flux of a neutral-like fluorescence line emitted locally from an illuminated disk is:

$$F_{fluorescence}(R) = \int_{\varepsilon_{Th}}^{\infty} F_{\varepsilon}^{continuum}(R) d\varepsilon (1 - e^{-\tau_{FeK}}) \omega$$

where ε_{Th} is the threshold energy for photoionization, τ_{FeK} is the optical depth at this energy and is assumed to be large, $F_{\varepsilon}^{continuum}(R)$ is the continuum flux, ω is the fluorescence yield and y_{Fe} is the iron abundance relative to solar (Grevesse et al., 1996). If we define the incident continuum flux in terms of the luminosity from the neutron star, L, the radius R,

a factor $f \leq 1$ which accounts for non-normal incidence, attenuation between the continuum source and the disk, etc., and a factor κ which is the fraction of the continuum flux absorbed by iron K, we can write:

$$\kappa f(R) \frac{L}{4\pi R^2} = \int_{\varepsilon_{Th}}^{\infty} F_{\varepsilon}^{continuum}(R) d\varepsilon$$

Then the total fluorescent line luminosity is obtained by integrating over the disk surface between two radii R_{min} and R_{max}:

$$L_{fluorescence} = \omega y_{Fe} \kappa \frac{L}{2} \int_{R_{min}}^{R_{max}} \frac{f(R)}{R} dR$$

If we take $f(R)$=constant, then

$$L_{fluorescence} \simeq \omega y_{Fe} \kappa \frac{L}{2} \ln(R_{max}/R_{min}) f$$

Taking plausible values for these quantities: ω=0.34 (valid for neutral-like iron), $y_{Fe} = 1$, κ=0.2 (for an ε^{-1} power law) $L = 3 \times 10^{35}$ erg s^{-1} (the measured value for a distance of 7 kpc), R_{max}/R_{min}=100 (an upper limit with little effect on the result), f=0.1 (an upper limit; cf. Ko and Kallman 1994), we get $L_{fluorescence} \simeq 5 \times 10^{33}$ erg s^{-1}. This is greater than the upper limit allowed by the observations for the 6.4 keV line, 1.8×10^{33} erg s^{-1}, suggesting that the illumination is weaker than we have assumed, $f \leq 0.03$, or that the iron abundance is less than solar.

5. Summary

The complementary capabilities of Chandra and XMM provide new insight into the reprocessing gas in 2S0921-630. The XMM RGS allows detection of line emission from elements such as oxygen, while the Chandra HETG allows detection of the K lines of sulfur and iron. The XMM EPIC detectors allow measurement of the spectrum above 7 keV and measurements of line widths. We have found line emission from medium-Z elements, O, Ne, Me, Si, S, and also K lines from iron. With the exception of the neutral-like and H-like components of the Fe K line as measured by the PN detector on XMM, the lines have widths which are less than can be measured with the Chandra and XMM detectors. The measured widths for the two components of the iron line suggest upper limits to the size of the ADC of 7×10^{10} cm for a 1 M$\odot$ compact object at 90^o inclination if orbital Doppler

broadening is the dominant mechanism. The line spectra from each grating instrument fit adequately with photoionized models. However, the XMM observations require a second component at lower ionization parameter than inferred for Chandra. The O VII lines are detected in the XMM RGS and imply gas densities in the range 10^9 – 10^{11} cm^{-3}, which in turn implies that either the X-ray source is intrinsically faint, that the emission region lies outside of the accretion disk, or that large regions of the ADC are very optically thick. The distribution of emission measures of xstar models which comes closest to fitting the ensemble of the line data is a 3 component model, similar to that inferred from the separate xstar fits to the Chandra and XMM grating data. The emission measures inferred from both a simple optically thin DEM analysis and from the xstar fits are consistent with simple estimates for an ADC if the intrinsic luminosity of the source is approximately what we observe. The high energy spectrum as observed by the PN shows complex structure at energies above 5 keV: curvature in the continuum spectrum, multiple iron Kα components similar to those seen in the Chandra HETG, plus either additional emission features at 7.8 keV and 8.2 keV, absorption, or reprocessed emission which differs from standard reflection models.

The picture of the ADC that we are left with is as follows: The total ADC emission measure is comparable to that obtained from simple estimates, although the distribution of ionization parameter is not smooth, monotonic, or easily predicted or compared with models. The width of the Fe XXVI Lα line implies that high ionization gas is distributed primarily at radii less than $\simeq 7 \times 10^{10}$cm. The intensity of the neutral-like Fe Kα line implies that this material is primarily at large radii, i.e. greater than $\simeq 10^9$cm. If so, the measured width of this line is due to blending of multiple components due to different ion stages. The constraints on the density of the O VII emitting gas require that either the intrinsic luminosity of the continuum source be low, i.e. $\leq 10^{36}$ erg s^{-1}, or that the O VII emitting region be heavily shielded from direct X-rays. The first scenario implies that we observe the full luminosity of the continuum source. This conflicts with ADC models in which the intrinsic luminosity of ADC source is much greater than we observe and that much of what we observe is scattered or diffused through the ADC. The second scenario requires a large column density ($\geq 10^{23}$ cm^{-2}) of absorbing or scattering gas which is not apparent from the observed spectrum. The high energy spectrum, above the iron K line region, shows evidence for complicated and unexplained emission, or possibly absorption. Although simple models for absorption do not fit the spectrum as well, both emission and absorption models produce fits which are statistically acceptable. The absorption scenario is more plausible owing to the likelihood of dense gas associated with the disk atmosphere, bulge, or wind impinging on the line of sight. If so, this gas is highly ionized and also has large column density ($\geq 10^{24}$ cm^{-2}). More sensitive observations, or more secure EPIC

calibration, in the 1-20 keV energy band may allow this to be tested; an absorption scenario would predict that the underlying power law would recover at energies ∼15 keV.

Acknowledgements This work was supported by grants from NASA through the Chandra and XMM guest observer programs.

REFERENCES

Arnaud, K.A., 1996, Astronomical Data Analysis Software and Systems V, eds. Jacoby G. and Barnes J., p17, ASP Conf. Series volume 101

Asai, K., Dotani, T., Nagase, F., and Mitsuda, K., 2000, Ap. J. Supp., 131, 571

Bautista, M., and Kallman, T., 2000, ApJ, 544, 581

Bautista, M., and Kallman, T., 2001, Ap. J. Supp., 133,221

Begelman, M., McKee, C., and Shields, 1982, Ap. J., 271, 70

Branduardi-Raymont, G., et al., 1981, Space Sci. Rev., 30, 279

Branduardi-Raymont, G., et al., 1981, MNRAS, 205, 403

Chevalier, C., and Ilovaisky, S., 1981, Astr. and Ap., 94, L3

Chevalier, C., and Ilovaisky, S., 1982, Astr. and Ap., 112, 68

Cottam, J., et al., 2001 ApJ, 557, 101

Cowley, A., et al., 1982, Ap. J., 256, 605

Frank, J., King, A., and Raine, D., 1992 'Accretion Power in Astrophysics', Cambridge Astrophysics Series (Cambidge University Press; Cambridge)

Gottwald, M ,et al. 1995, A. and A. Supp., 109, 9

Grevesse, N., Noels, A., and Sauval, A. 1996, in ASP Conf. Ser. 99, Cosmic Abundances, ed. S. Holt and G. Sonneborn (San Francisco: ASP), 117

Jimenez-Garate, M., et al., 2001, ApJ, 558, 448

Kallman, T., and Bautista, M., 2001, ApJS, 133, 221

Kallman, T., and White, N., 1989, Ap. J., 341, 955

Kallman, T., Liedahl, D., Osterheld, A., Goldstein, W., and Kahn, S., 1996, Ap., J., 465, 994

Ko, Y., and Kallman, T., 1994, Ap. J., 431, 273

Krolik, J., McKee, C., and Tarter, C. B., 1981, Ap. J. 249, 422

Mason, K., et al., 1987, MNRAS, 226, 423

Mason, K. O., 1986, in, Physics of Accretion onto Compact Objects,, p.29, eds Mason, Watson, and White, Springer-Verlag, Heidelberg

McClintock, J., et al., 1982, Ap. J., 258, 245

Porquet, D., and Dubau, J., 2000, A and AS, 143, 495

Proga, D., and Kallman, T., 2002, ApJ, 565, 455

Shahbaz, T., et al., 1999, Ast. Ap., 344,101

Vrtilek, S., Soker, N., and Raymond, J., 1994, Ap. J., 404, 696

Verner, D. A., Verner, E. M. and Ferland, G. J., 1996, Atomic Data Nucl. Data Tables, 64, 1

White, N.E., and Holt, S., 1982, Ap. J., 257, 318

White, N.E., 1996, in, X-Ray Imaging and Spectroscopy of Cosmic Hot Plasmas,, ed. F. Makino

Woods, D., et al., 1996, ApJ, 461, 767

Appendix

The general procedure for inferring the emission measure from the normalization calculated using the fit to the xstar model is as follows. The observational data is fitted to a library of xstar table models constructed using the xstar2xspec tool. When this library was calculated a source luminosity L_{xstar} was used, and when the data was fitted to the model a best fit normalization, xstar ionization parameter (ξ) and column density (N) were derived. The best-fit xstar model was calculated as a spherical shell, and its emission measure is

$$EM_{xstar} = n^2 4\pi R^2 \Delta R = 4\pi \frac{L_{xstar} N}{\xi}$$

If the distance to the source (D) and its intrinsic luminosity (L) are known, then the emission measure of the source is given by

$$EM = \text{normalization} \times EM_{xstar} \left(\frac{L_{xstar}}{L} 4\pi D_{kpc}^2 \right)$$

where D_{kpc} is the distance to the source in kpc.

In the case of the fit to the Chandra HETG spectrum the best fit normalization is 210, for an ionization parameter $\xi \simeq 10^5$, and $L_{xstar} = 10^6$ and $EM_{xstar} = 2 \times 10^{61}$. This corresponds to a source emission measure of $EM = 6.8 \times 10^{54}$ cm^{-3} L_{38}^{-1} D_7^2, where L_{38} is the continuum luminosity in units of 10^{38} erg s^{-1} and D_7 is the distance in units of 7 kpc.

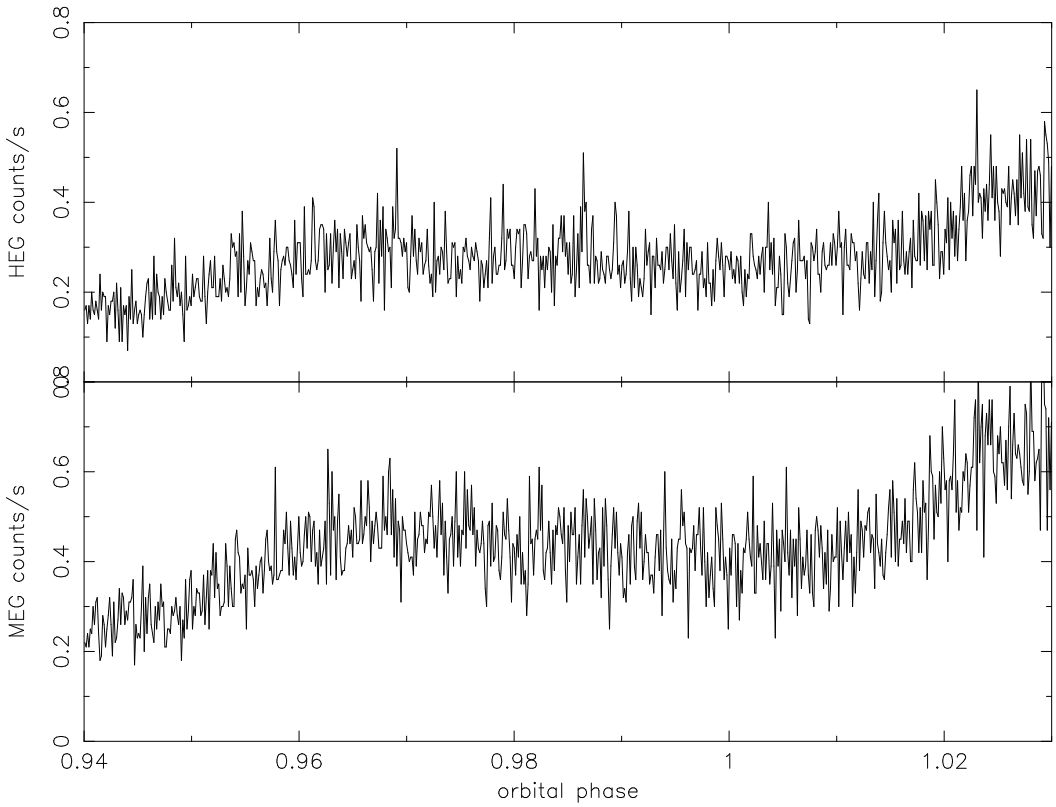

Fig. 1.— HEG light curve during the Chandra Observation of 2S0921-63 plotted vs. orbital phase in 100 second time bins

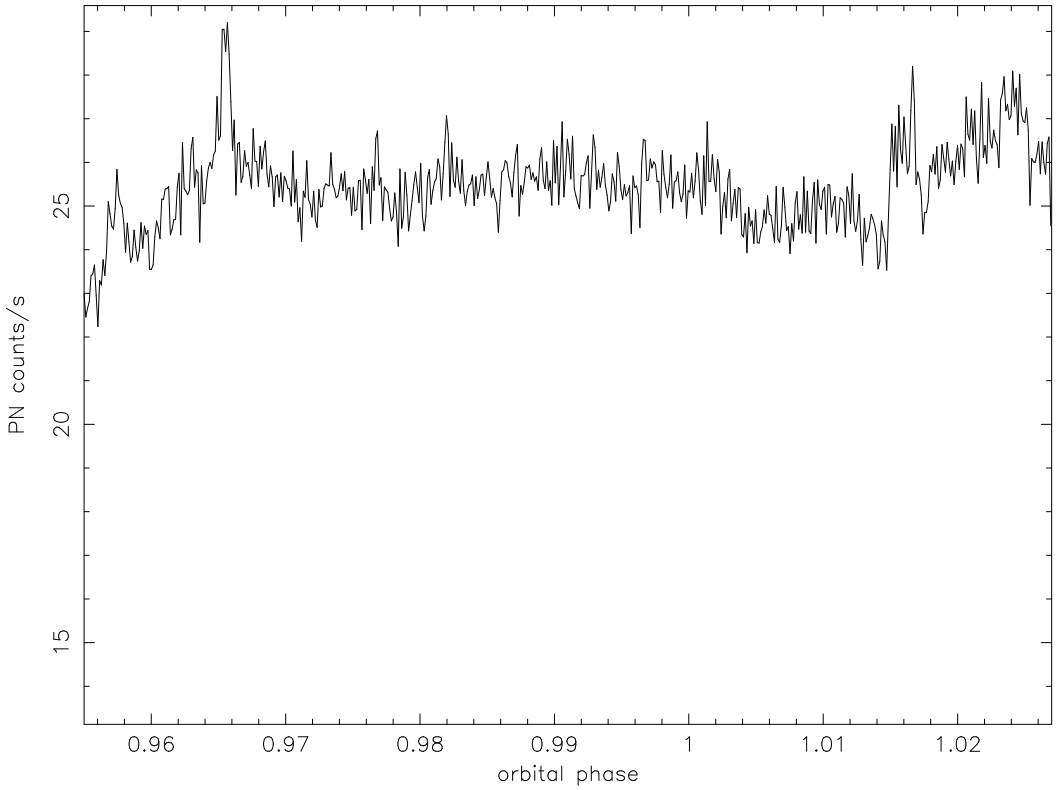

Fig. 2.— PN Light curve during the XMM Observation of 2S0921-63 plotted vs. orbital phase in 1 second time bins.

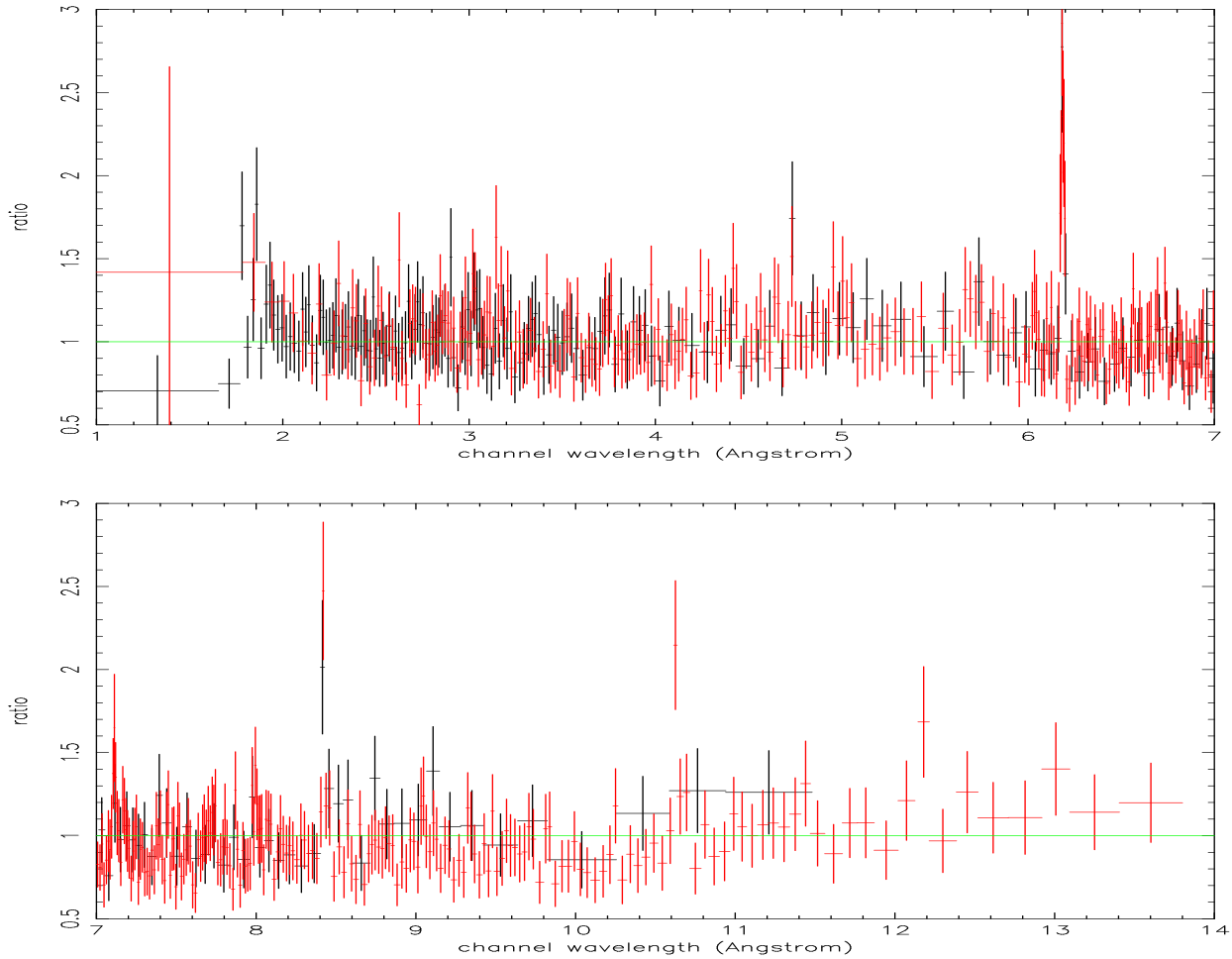

Fig. 3.— Ratio of HETG spectrum to absorbed power law model. HEG (read) and MEG (black) are displayed separately.

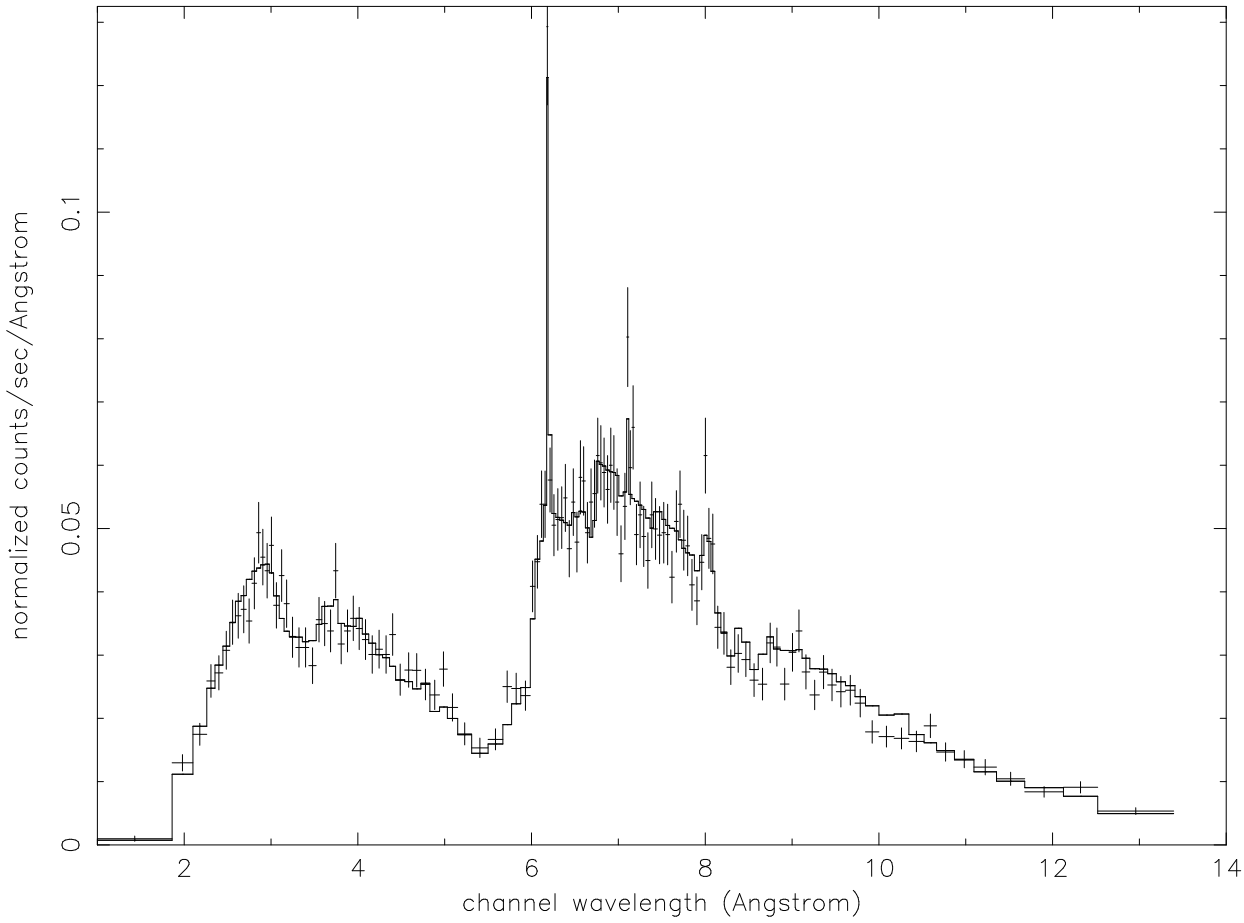

Fig. 4.— Xstar model fit to HETG spectrum. Only the HEG is shown for clarity.

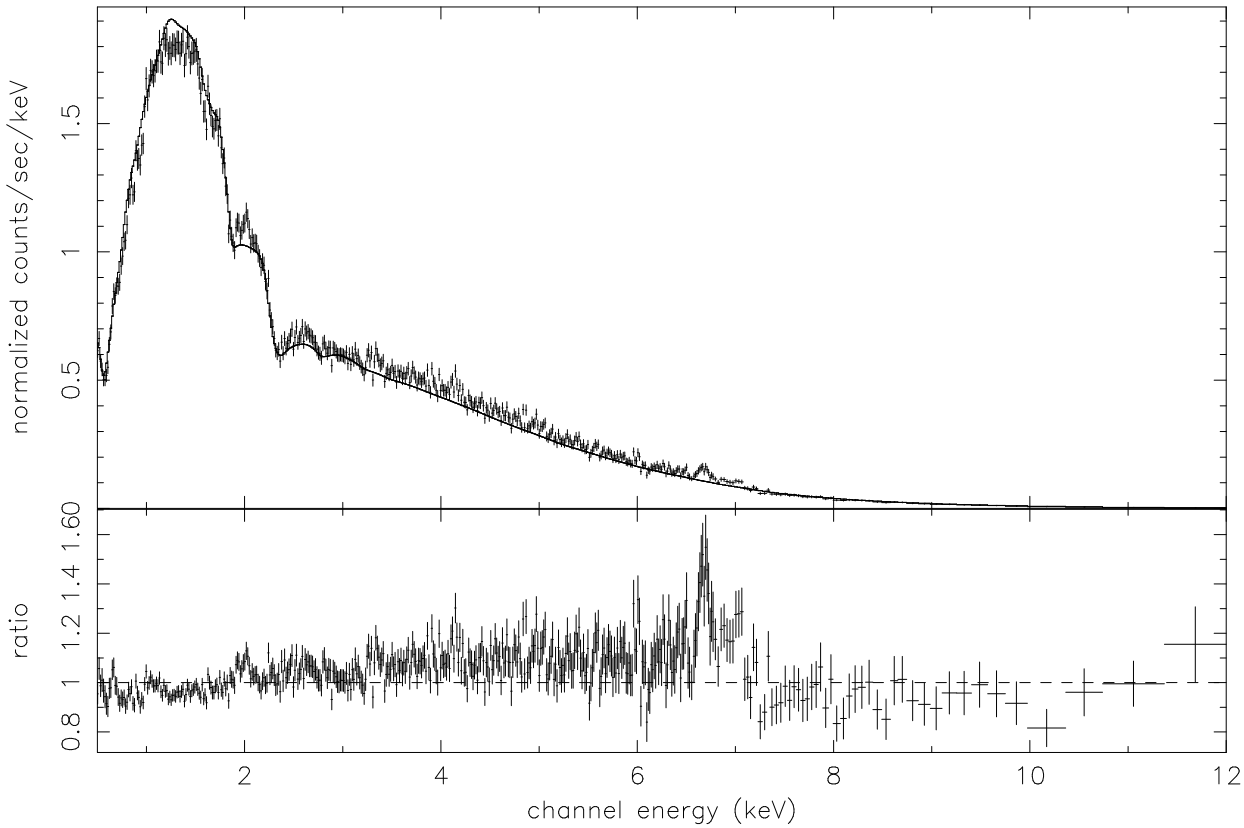

Fig. 5.— EPIC-MOS spectrum, counts + model (upper panel) and counts/model ratio (lower panel). Only MOS 1 is shown for clarity.

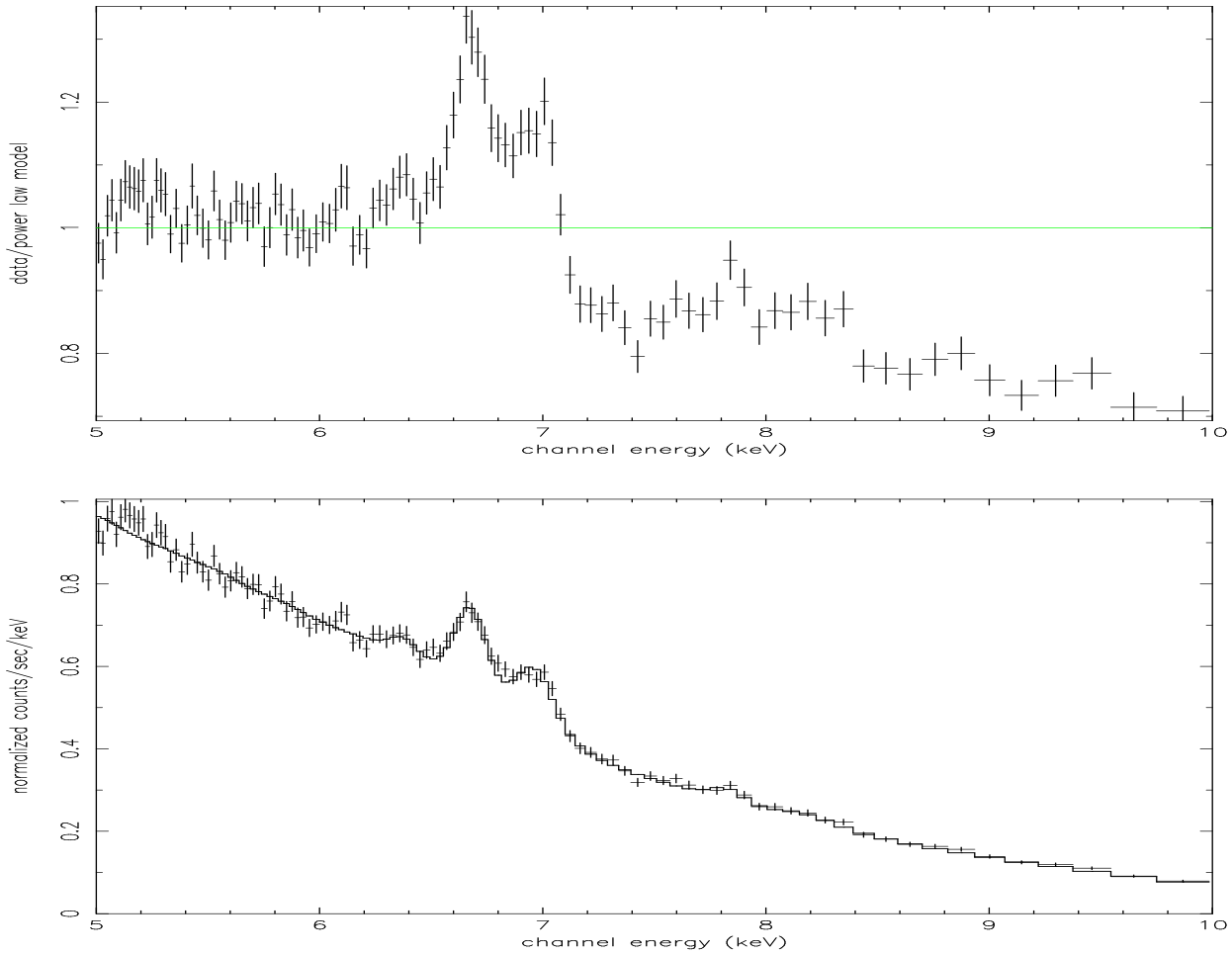

Fig. 6.— EPIC PN spectrum in the vicinity of the iron K line, Upper panel: Ratio of data to cutoff power law model. Lower panel: Fit to cutoff power law plus Gaussian emission lines and edge.

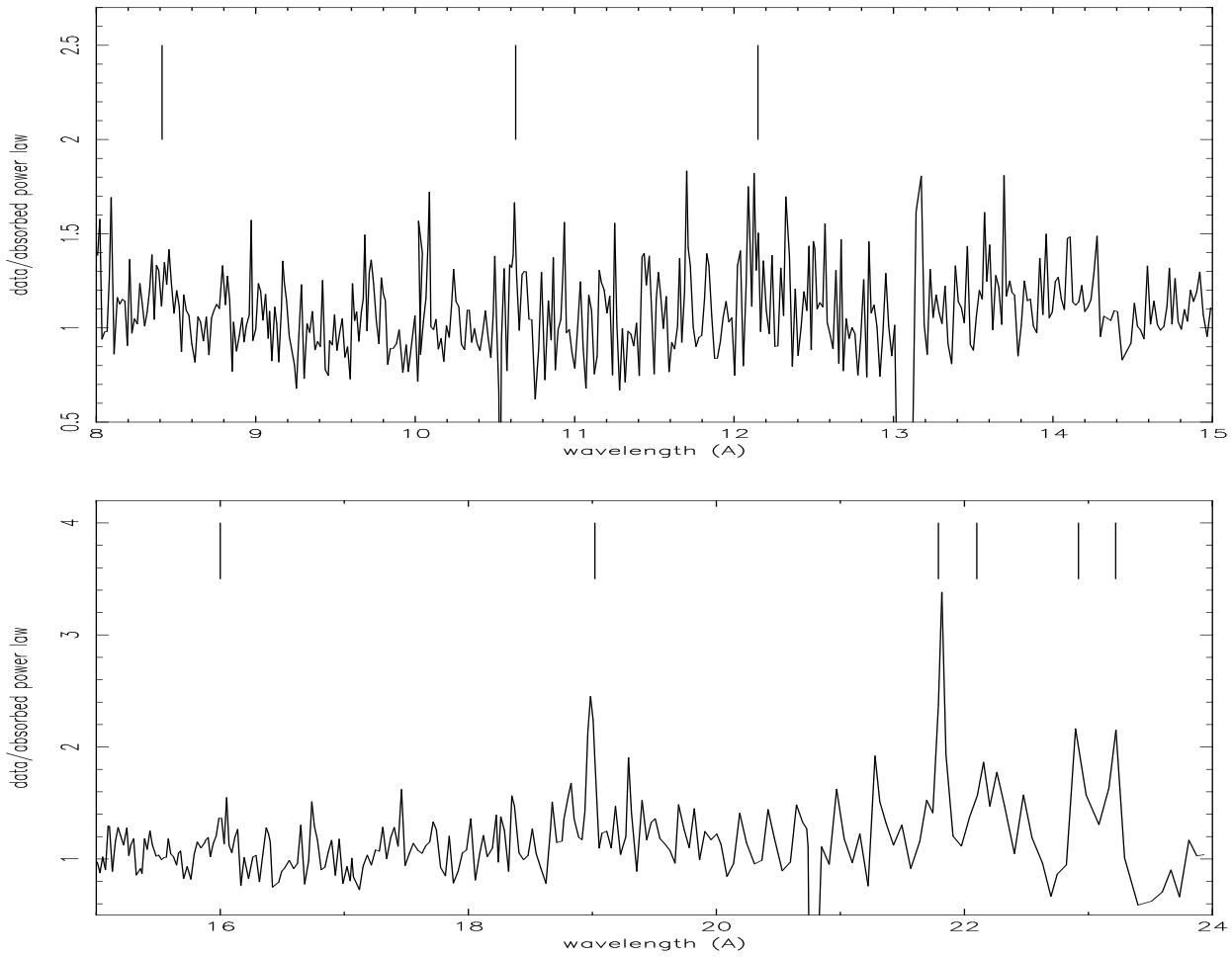

Fig. 7.— Ratio of RGS spectrum to absorbed power law model. Strong lines are marked with vertical bars. RGS 1 and RGS 2 have been combined

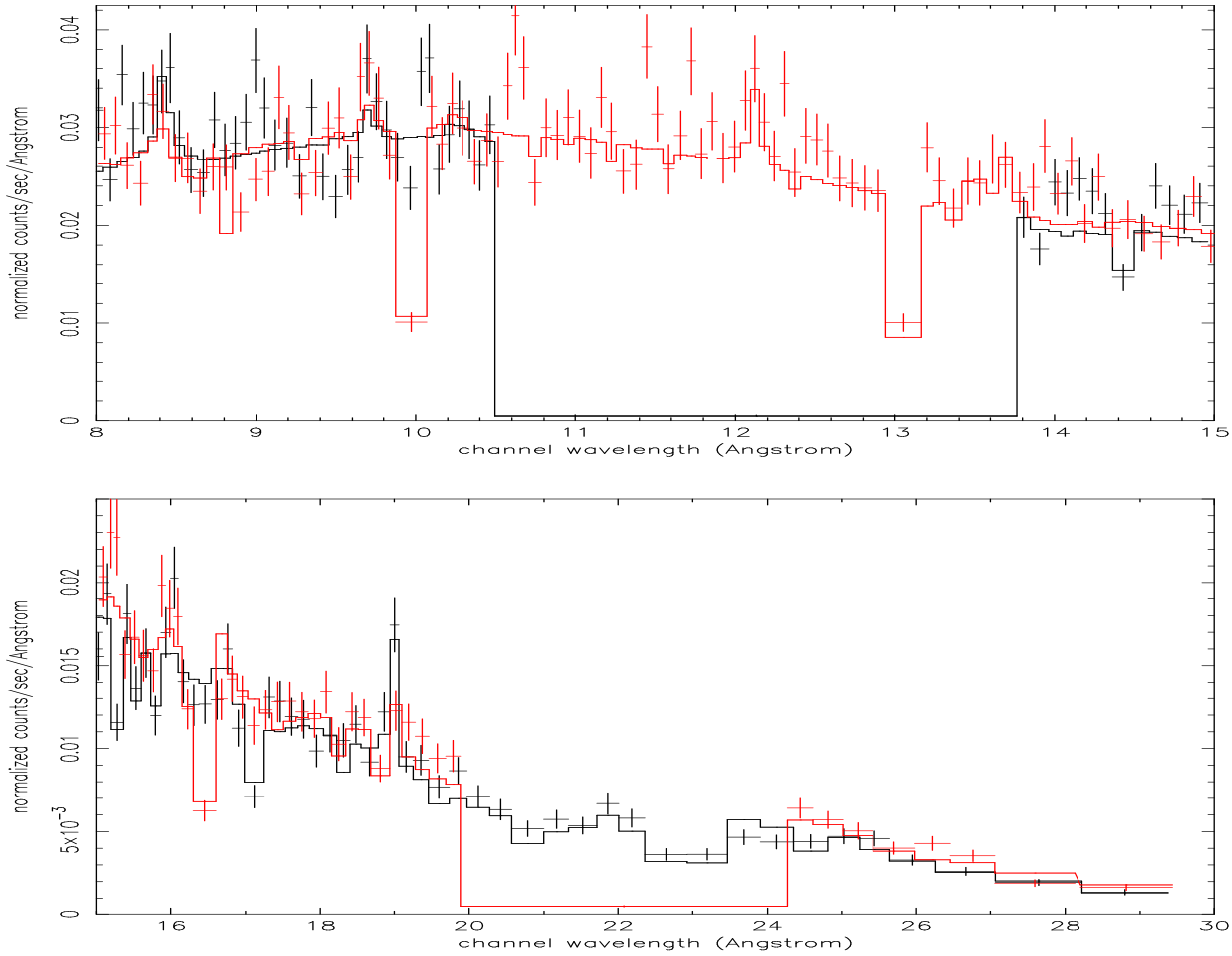

Fig. 8.— Xstar model fit to RGS spectrum using 2 component model as described in the text. RGS 1 and RGS 2 are plotted separately. Upper panel: 8 – 15 $\AA$ (0.8 – 1.6 keV) range. Lower panel: 15 – 30 $\AA$ (0.4 – 0.8 keV) range.

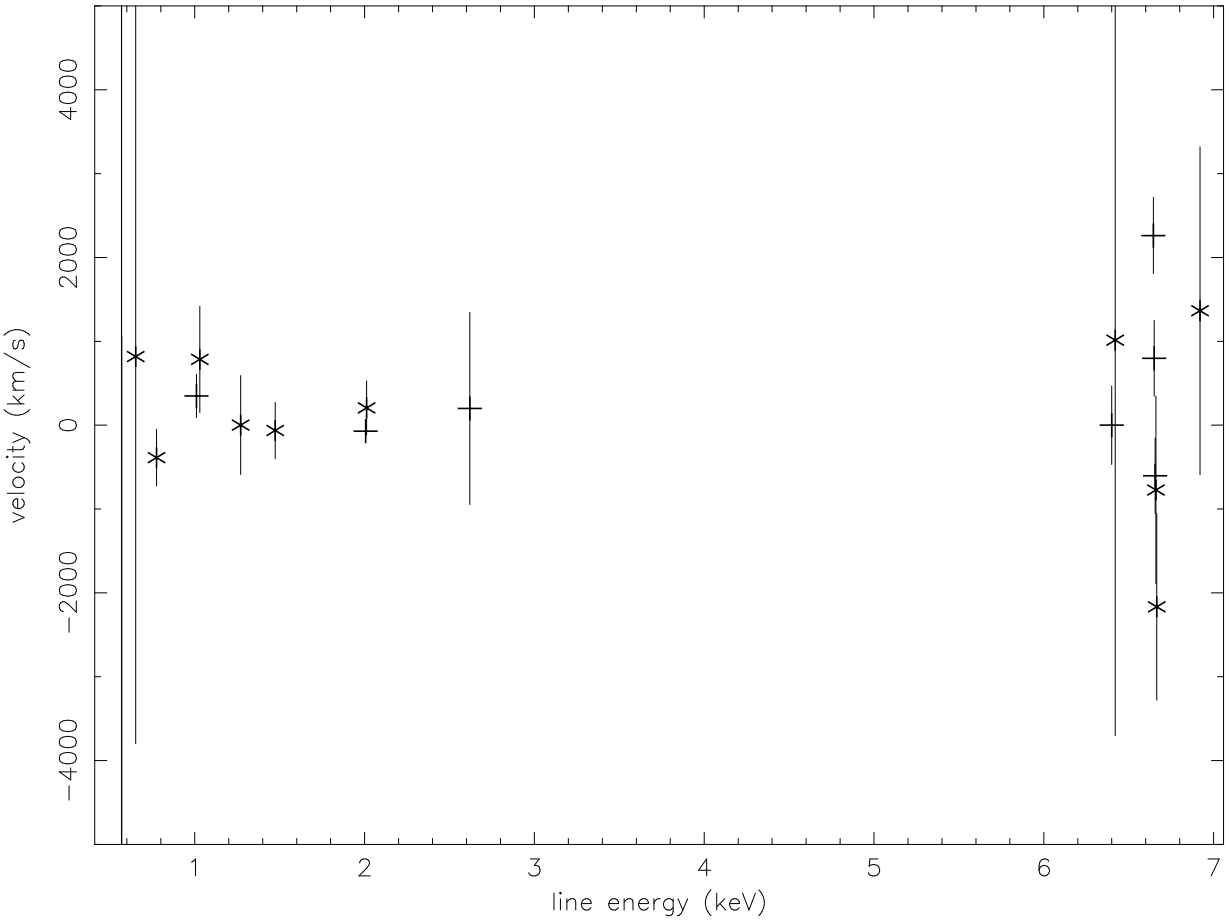

Fig. 9.— Comparison of line velocities derived from XMM (*) and Chandra (+)

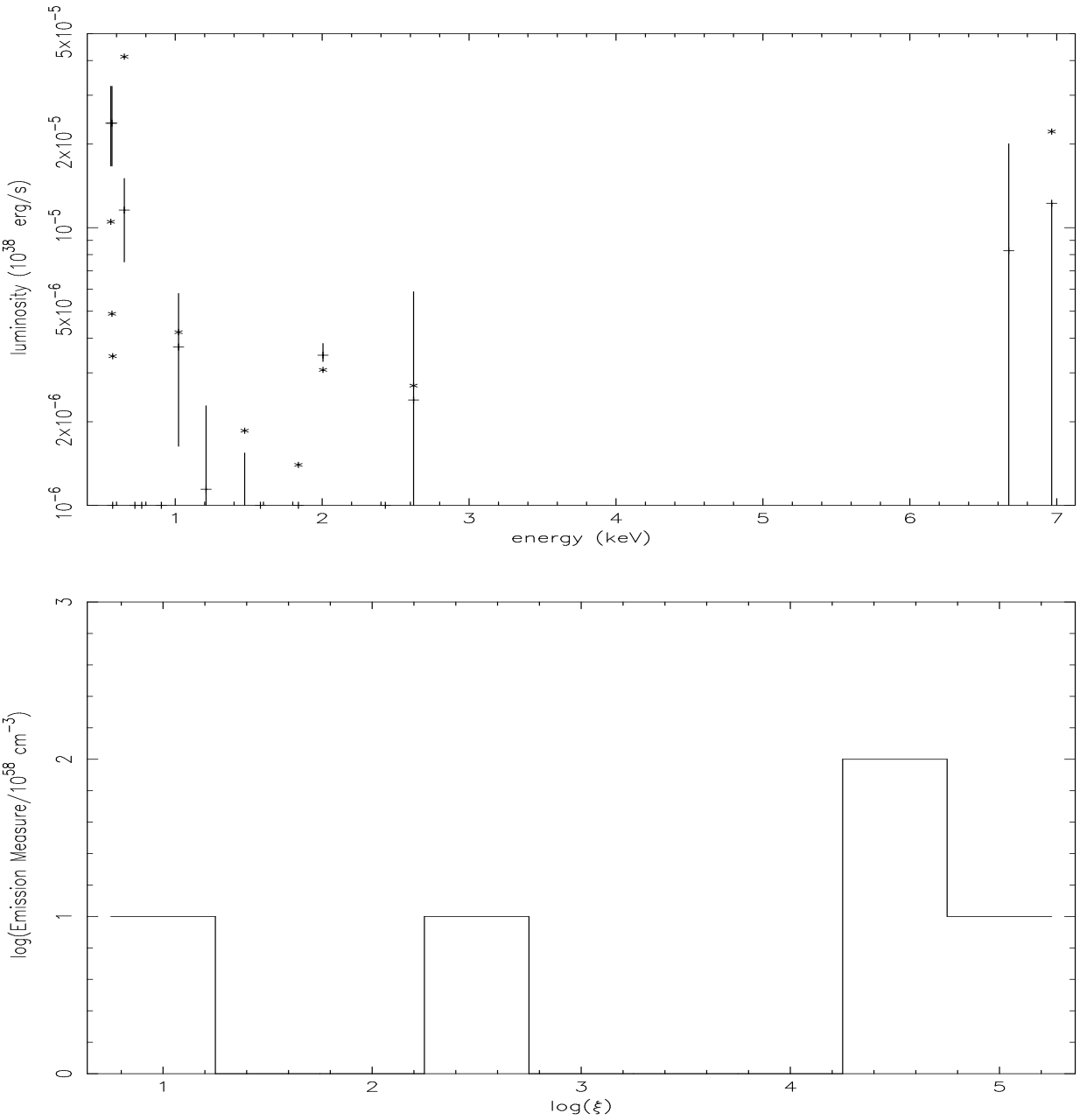

Fig. 10.— Upper panel: Comparison of line luminosities derived from XMM and Chandra (+) with the result of a differential emission measure fit to the data using xstar models (*). Lower panel: best fit emission measure distribution

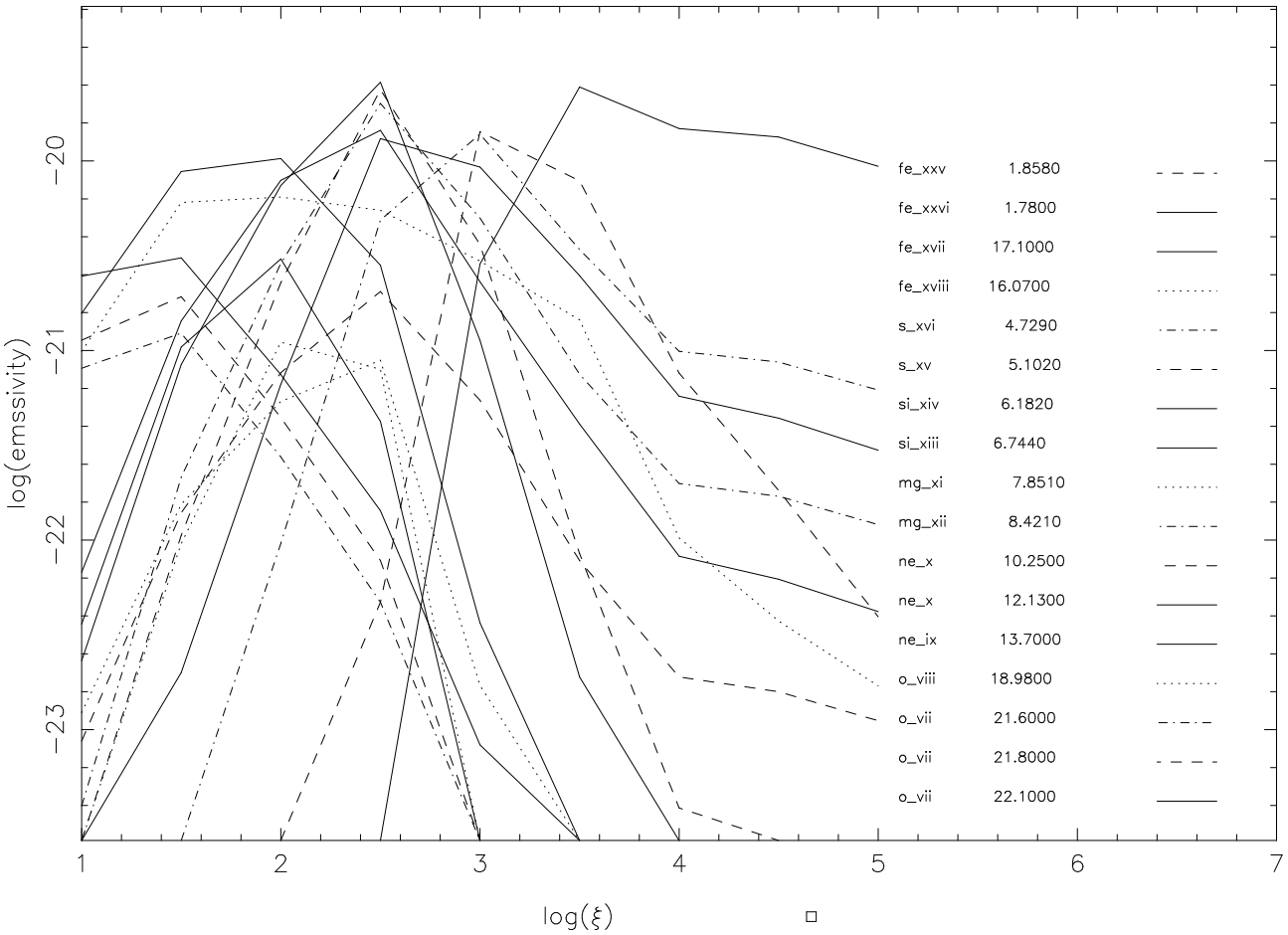

Fig. 11.— Emissivities in erg cm^3 s^{-1} for strong lines in the Chandra/XMM band as calculated by xstar

Table 1. ASCA Lines

quantity	value
Absorption, NH ($\times 10^{22}$ cm^{-2})	0.17
Power Law Index (photons)	1.1
Cutoff Energy (keV)	17.8
normalization (erg cm^{-2} s^{-1})	$4.0^{+}_{-}0.1 \times 10^{-3}$
Flux 2-11 keV (erg cm^{-2} s^{-1})	3.45×10^{-11}
line 1	
Wavelength ($\AA$)	12.4
Energy (keV)	$1.0^{+0.02}_{-0.75}$
normalization ($\times 10^{-5}$erg cm^{-2} s^{-1})	$9.7^{+10.}_{-6.}$
Equivalent Width (eV)	$22^{+}_{-}8$
Line ID	Ne X Lα
log(P)	-4.3
line 2	
Wavelength ($\AA$)	10.7
Energy (keV)	$1.15^{+0.05}_{-0.08}$
normalization ($\times 10^{-5}$erg cm^{-2} s^{-1})	$4.7^{+5.}_{-4.}$
Equivalent Width (eV)	$22^{+}_{-}8$
Line ID	Ne X Lβ
log(P)	-3.0

Table 1. ASCA Lines, continued

quantity	value
line 3	
Wavelength ($\mathring{A}$)	6.2
Energy (keV)	$1.99^{+}_{-}0.1$
normalization ($\times 10^{-5}$erg cm^{-2} s^{-1})	$3.5^{+3.}_{-2.}$
Equivalent Width (eV)	$20^{+}_{-}11$
Line ID	Si XIV Lα
log(P)	-2.2
line 4	
Wavelength ($\mathring{A}$)	4.77
Energy (keV)	$2.6^{+}_{-}0.1$
normalization ($\times 10^{-5}$erg cm^{-2} s^{-1})	1.5^{+2}_{-2}
Equivalent Width (eV)	$15^{+}_{-}9$
Line ID	S XVI Lα
log(P)	-0.32
line 5	
Wavelength ($\mathring{A}$)	1.82
Energy (keV)	$6.8^{+}_{-}0.1$
normalization ($\times 10^{-5}$erg cm^{-2} s^{-1})	$4.7^{+2.3}_{-3.7}$
Line ID	Fe K
log(P)	-3.49
Equivalent Width (eV)	$115^{+}_{-}40$
χ^2/PHA bins	718/595

Table 2. Results of fitting to Chandra HETG

Parameter	Power Law Only	Power Law + Gaussian
NH ($\times 10^{21}$ cm^{-2})	1.6	1.6
photon index	$1.00^{+0.15}_{-0.9}$	$1.09^{+0.15}_{-0.9}$
normalization(erg cm^{-2} s^{-1})	$.0031^{+.0007}_{-.0006}$	$.0033^{+.0007}_{-.0006}$
line 1		
wavelength ($\AA$)	–	12.16
energy (keV)	–	$1.02^{+0.0015}_{-0.00025}$
normalization ($\times 10^{-5}$erg cm^{-2} s^{-1})	–	$2.4^{+2}_{-1.5}$
equivalent width (eV)	–	6.65
ID	–	Ne X Lα
log(P)	–	-19.2
line 2		
wavelength ($\AA$)	–	10.60
energy (keV)	–	$1.17^{+}_{-}0.01$
normalization ($\times 10^{-5}$erg cm^{-2} s^{-1})	–	$1.1^{+1.2}_{-0.8}$
equivalent width (eV)	–	3.52
ID	–	Ne X Lβ
log(P)	–	-7.74
line 3		
wavelength ($\AA$)	–	8.56
energy (keV)	–	$1.45^{+}_{-}0.0025$
normalization ($\times 10^{-5}$erg cm^{-2} s^{-1})	–	$7.0^{+5}_{-5.}$
equivalent width (eV)	–	0.185
ID	–	Mg XII Lα
log(P)	–	-0.06
line 4		
wavelength ($\AA$)	–	6.18
energy (keV)	–	$2.006^{+0.0003}_{-0.004}$
normalization ($\times 10^{-5}$erg cm^{-2} s^{-1})	–	$1.95^{+0.1}_{-0.2}$
equivalent width (eV)	–	10.2
ID	–	Si XIV Lα
log(P)	–	-34.3
line 5		
wavelength ($\AA$)	–	4.73
energy (keV)	–	$2.62^{+}_{-}0.01$
normalization ($\times 10^{-5}$erg cm^{-2} s^{-1})	–	$1.03^{+1.5}_{-1.}$
equivalent width (eV)	–	13.2
ID	–	S XVI Lα
log(P)	–	-4.09

Table 2. Results of fitting to Chandra HETG, continued

Parameter	Power Law Only	Power Law + Gaussian
line 6		
wavelength ($\AA$)	–	1.938
energy (keV)	–	$6.400^{+}_{-}0.01$
normalization ($\times 10^{-5}$erg cm^{-2} s^{-1})	–	$1.1^{+}_{-}2$
equivalent width (eV)	–	26.2
ID	–	Fe neutral-like Kα
log(P)	–	-2.03
line 7		
wavelength ($\AA$)	–	1.865
energy (keV)	–	$6.650^{+}_{-}0.01$
normalization ($\times 10^{-5}$erg cm^{-2} s^{-1})	–	$1.4^{+}_{-}2$
equivalent width (eV)	–	31.1
ID	–	Fe XXV 1-2
log(P)	–	-3.28
line 8		
wavelength ($\AA$)	–	1.797
energy (keV)	–	$6.900^{+}_{-}0.01$
normalization ($\times 10^{-5}$erg cm^{-2} s^{-1})	–	≤ 2
equivalent width (eV)	–	50.1
ID	–	Fe XXVI Lα
log(P)	–	-0.2
C statistic/PHA bins	9390/8384	9009/8384

Table 3. Results of fitting to Chandra HETG with xstar table + power law model

Parameter	Value
NH ($\times 10^{21}$ cm^{-2})	2.0
photon index	$1.03^{+0.15}_{-0.9}$
normalization (erg cm^{-2} s^{-1})	$.00286^{+.0007}_{-.0006}$
xstar column density	10^{21} cm^{-2}
log(ξ)	4.5
xstar normalization	300.0^{+300}_{-200}
C statistic/PHA bins	8731/8384

Table 4. Results of fitting to XMM EPIC MOS

Parameter	Power Law only	power law + Gaussian
NH ($\times 10^{21}$ cm^{-2})	$1.735^{+}_0.05$	$1.757^{+}_0.05$
photon index	1.184+_0.01	1.193+_0.01
normalization ($\times 10^{-3}$ erg cm^{-2} s^{-1}	$6.7^{+}_0.15$	$6.78^{+}_0.15$
line 1		
wavelength ($\AA$)	–	1.85
energy (keV)	–	$6.698^{+}_0.1$
normalization ($\times 10^{-5}$erg cm^{-2} s^{-1})	–	$4.0^{+}_1.0$
equivalent width (eV)	–	1500
ID	–	Fe XXV 1 – 2
log(P)	–	-7.5
line 2		
wavelength ($\AA$)	–	1.78
energy (keV)	–	$6.978^{+}_0.1$
normalization ($\times 10^{-5}$erg cm^{-2} s^{-1})	–	$1.2^{+}_1.0$
equivalent width (eV)	–	288
ID	–	Fe XXVI Lα
log(P)	–	-1.95
χ^2/ν	2077/1209	1969/1203

Table 5. Results of fitting to XMM EPIC PN

Parameter	Power Law Only	Power Law + Gaussian
NH ($\times 10^{21}$ cm^{-2})	6.6	11.2
photon index	1.2	1.2
High Energy Cutoff (keV)	–	7
normalization (erg cm^{-2} s^{-1})	.0112$^{+}_{-}$0.005	.0116$^{+}_{-}$.0003
line 1		
wavelength ($\AA$)	–	1.94
energy (keV)	–	6.38$^{+}_{-}$0.1
width (keV)	–	0.29$^{+}_{-}$0.15
normalization ($\times 10^{-5}$erg cm^{-2} s^{-1})	–	$1.4^{+0.15}_{-0.05}$
equivalent width (eV)	–	14
ID	–	Fe I – XVII Kα
log(P)	–	-99.
line 2		
wavelength ($\AA$)	–	1.86
energy (keV)	–	6.68$^{+}_{-}$0.03
width (keV)	–	$\leq$0.1 keV
normalization ($\times 10^{-5}$erg cm^{-2} s^{-1})	–	5.7$^{+}_{-}$0.2
equivalent width (eV)	–	63
ID	–	Fe XXV 1-2
log(P)	–	-5.59

Table 5. Results of fitting to XMM EPIC PN, continued

Parameter	Power Law Only	Power Law + Gaussian
line 3		
wavelength ($\AA$)	–	1.78
energy (keV)	–	$6.96^{+0.02}_{-0.07}$
width (keV)	–	$0.05^{+}_{-}0.04$
normalization ($\times 10^{-5}$erg cm^{-2} s^{-1})	–	$4.0^{+}_{-}0.1$
equivalent width (eV)	–	49
ID	–	Fe XXVI Lα
log(P)	–	-99.
line 4		
wavelength ($\AA$)	–	1.59
energy (keV)	–	$7.8^{+}_{-}0.1$
width (keV)	–	≤ 0.5
normalization ($\times 10^{-5}$erg cm^{-2} s^{-1})	–	$1.3^{+}_{-}0.3$
equivalent width (eV)	–	23
ID	–	–
log(P)	–	-3.74
line 5		
wavelength ($\AA$)	–	1.51
energy (keV)	–	$8.2^{+}_{-}0.1$
width (keV)	–	≤ 0.3
normalization ($\times 10^{-5}$erg cm^{-2} s^{-1})	–	$1.4^{+}_{-}0.3$
equivalent width (eV)	–	25
ID	–	–
log(P)	–	-5.58
χ^2/ν	2074/1039	874/1028

Table 6. Results of fitting to EPIC RGS

Parameter	Power Law Only	Power Law + Gaussians
NH ($\times 10^{21}$ cm^{-2})	2.1	2.1
photon index	1.2	1.2
normalization (erg cm^{-2} s^{-1})	.0085$\pm$0.0001	.0085$\pm$0.0001
line 1		
wavelength ($\AA$)	–	23.22
energy (keV)	–	0.534$\pm$0.01
normalization ($\times 10^{-5}$erg cm^{-2} s^{-1})	–	5.3$\pm$7
equivalent width (eV)	–	2.8
ID	–	–
log(P)	–	-1.06
line 2		
wavelength ($\AA$)	–	22.92
energy (keV)	–	0.541$\pm$0.01
normalization ($\times 10^{-5}$erg cm^{-2} s^{-1})	–	7.1$\pm$8
equivalent width (eV)	–	3.5
ID	–	–
log(P)	–	-1.34
line 3		
wavelength ($\AA$)	–	22.10
energy (keV)	–	0.561$\pm$0.01
normalization ($\times 10^{-5}$erg cm^{-2} s^{-1})	–	4.5$\pm$5
equivalent width (eV)	–	2.2
ID	–	O VII $1s^2(^1S)$-1s2s(^{3}S)
log(P)	–	-1.15
line 4		
wavelength ($\AA$)	–	21.77
energy (keV)	–	0.569$\pm$0.01
normalization ($\times 10^{-5}$erg cm^{-2} s^{-1})	–	5.9$\pm$12
equivalent width (eV)	–	3.3
ID	–	O VII $1s^2(^1S)$-1s2p(^{3}P)
log(P)	–	-2.27

Table 6. Results of fitting to EPIC RGS, continued

Parameter	Power Law Only	Power Law + Gaussians
line 5		
wavelength ($\AA$)	–	19.0
energy (keV)	–	$0.652^{+}_{-}0.01$
normalization ($\times 10^{-5}$erg cm^{-2} s^{-1})	–	$7.6^{+}_{-}2$
equivalent width (eV)	–	5.4
ID	–	O VIII Lα
log(P)	–	-14.35
line 6		
wavelength ($\AA$)	–	15.97
energy (keV)	–	$0.775^{+0.0015}_{-0.00025}$
normalization ($\times 10^{-5}$erg cm^{-2} s^{-1})	–	$1.4^{+}_{-}2$
equivalent width (eV)	–	1.2
ID	–	O VIII Lβ
log(P)	–	-0.84
line 7		
wavelength ($\AA$)	–	12.13
energy (keV)	–	$1.021^{+0.0003}_{-0.004}$
normalization ($\times 10^{-5}$erg cm^{-2} s^{-1})	–	$3.6^{+2.3}_{-2.3}$
equivalent width (eV)	–	3.8
ID	–	Ne X Lα
log(P)	–	-2.17
line 8		
wavelength ($\AA$)	–	10.65
energy (keV)	–	$1.167^{+0.0003}_{-0.004}$
normalization ($\times 10^{-5}$erg cm^{-2} s^{-1})	–	$2.0^{+1.5}_{-0.}$
equivalent width (eV)	–	2.9
ID	–	Ne X Lβ
log(P)	–	-0.60
line 9		
wavelength ($\AA$)	–	8.40
energy (keV)	–	$1.474^{+0.0003}_{-0.004}$
normalization ($\times 10^{-5}$erg cm^{-2} s^{-1})	–	$4.0^{+2.7}_{-2.7}$
equivalent width (eV)	–	7.3
ID	–	Mg XII Lα
log(P)	–	-3.09
χ^2/ν	1522/1672	1393/1650

Table 7. Results of fitting to XMM RGS with xtar table + power law model

Parameter	Value
NH ($\times 10^{21}$ cm^{-2})	2.2
photon index	1.2
normalization (erg cm^{-2} s^{-1})	$.0081^{+.0007}_{-.0006}$
xstar column density	10^{21} cm^{-2}
xstar density	10^{11} cm^{-2}
Component 1	
log(ξ)	1
xstar normalization	2.0×10^{-4}
Component 2	
log(ξ)	4.5
xstar normalization	26.9
χ^2/ν	1413/1670

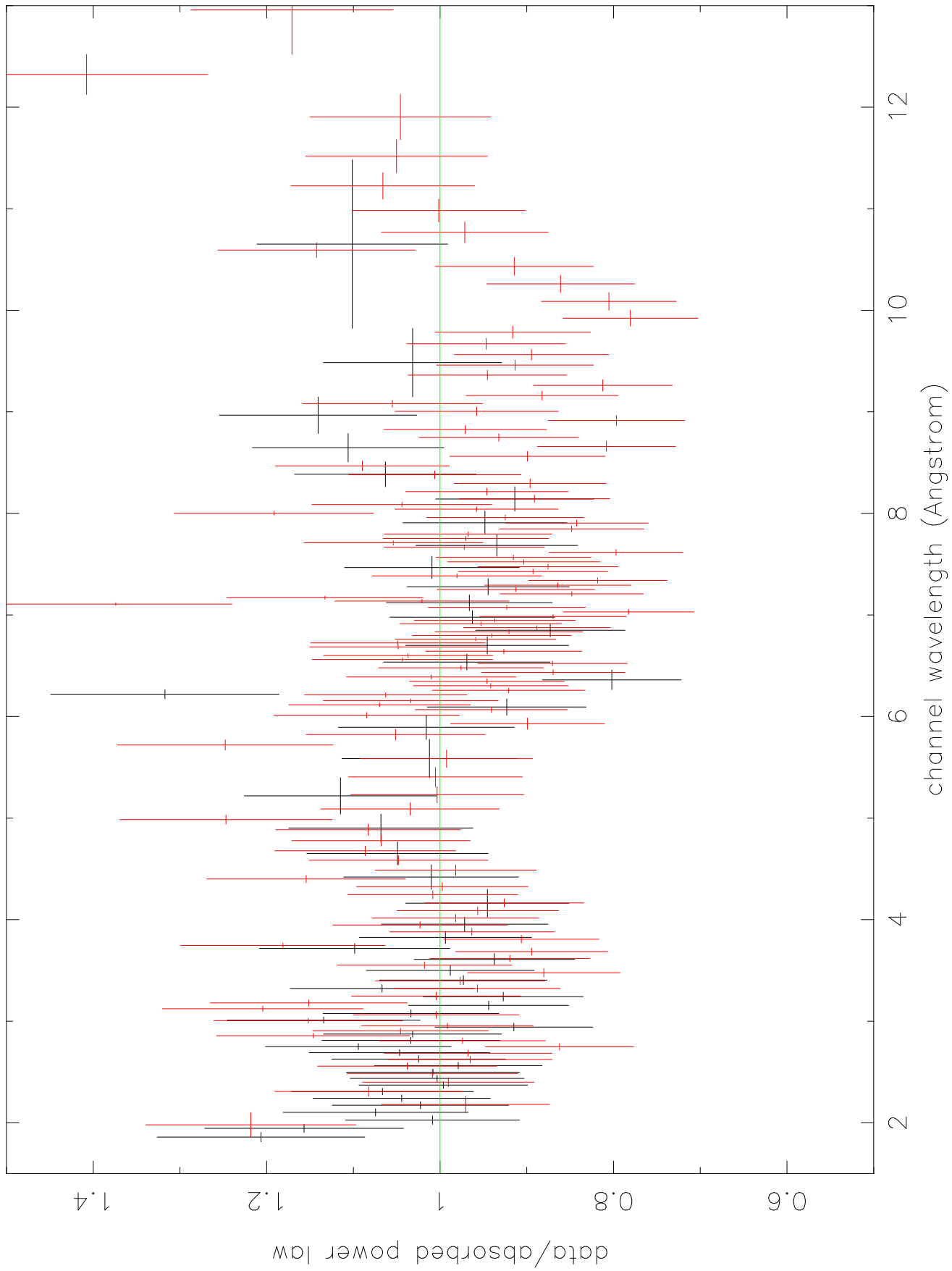
data/absorbed power law
0.6
0.8
1
1.2
1.4
channel wavelength (Angstrom)
2
4
6
8
10
12

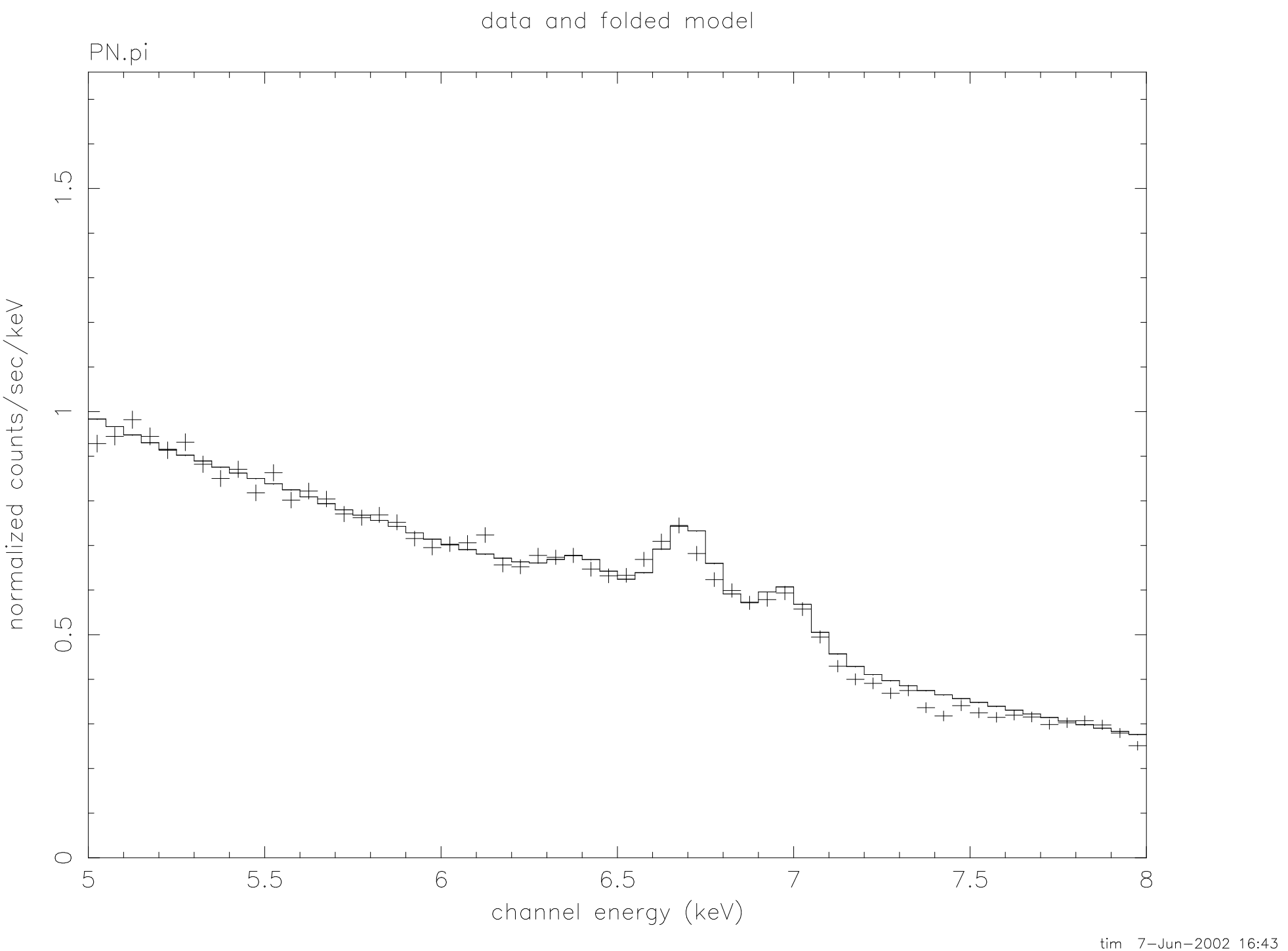
data and folded model
PN.pi
normalized counts/sec/keV
0
0.5
1
1.5
5
5.5
6
6.5
7
7.5
8
channel energy (keV)
tim 7-Jun-2002 16:43